A model study of the seasonal mixed layer heat budget in the equatorial Atlantic

Anne-Charlotte Peter,[1] Matthieu Le Hénaff,[2] Yves du Penhoat,[1] Christophe E. Menkes,[2] Frédéric Marin,[1] Jérôme Vialard,[2] Guy Caniaux,[3] and Alban Lazar[2]

Received 11 July 2005; revised 12 November 2005; accepted 17 February 2006; published 13 June 2006.

[1] In the present study, the physical processes that control the seasonal cycle of sea surface temperature in the tropical Atlantic Ocean are investigated. A high-resolution ocean general circulation model is used to diagnose the various contributions to the mixed layer heat budget. The simulation reproduces the main features of the circulation and thermal structure of the tropical Atlantic. A close examination of the mixed layer heat budget is then undertaken. At a first order, the mixed layer temperature balance in the equatorial band results from cooling by vertical processes and heating by atmospheric heat fluxes and eddies (mainly tropical instability waves). Cooling by subsurface processes is the strongest in June–August, when easterlies are strong, with a second maximum in December. Heating by the atmosphere is maximum in February–March and September–October, whereas eddies are most active in boreal summer. Unlike previous observational studies, horizontal advection by low-frequency currents plays here only a minor role in the heat budget. Off equator, the sea surface temperature variability is mainly governed by atmospheric forcing all year long, except in the northeastern part of the basin where strong eddies generated at the location of the thermal front significantly contribute to the heat budget in boreal summer. Finally, comparisons with previously published heat budgets calculated from observations show good qualitative agreement, except that subsurface processes dominate the cooling over zonal advection in the present study.

Citation: Peter, A.-C., M. Le Hénaff, Y. du Penhoat, C. E. Menkes, F. Marin, J. Vialard, G. Caniaux, and A. Lazar (2006), A model study of the seasonal mixed layer heat budget in the equatorial Atlantic, *J. Geophys. Res.*, *111*, C06014, doi:10.1029/2005JC003157.

1. Introduction

[2] The tropical Atlantic Ocean is a place of strong air-sea interactions, and much of the upper ocean variability is associated with the meridional displacement of the Inter-Tropical Convergence Zone (ITCZ), which modulates the trade winds [*Xie and Carton*, 2004]. Contrary to the Pacific Ocean where the El Niño Southern Oscillation signal dominates the variability, the annual cycle prevails in the Atlantic Ocean. One striking feature of the seasonal cycle is the appearance at the surface of cold water in boreal spring in the vicinity of the equator. This cold tongue appears from the coast of Africa, extending to roughly 15°W when the ITCZ moves northward in boreal spring, and reaches its maximum in June at 10°W at the equator [*Carton and Zhou*, 1997]. Sea Surface Temperature (SST) thus exhibits a marked seasonal signal, which amplitude can reach up to 7°C [*Houghton and Colin*, 1986] in the eastern part of the equatorial basin. The resulting temperature gradient between the cold water along the equator and the warmer water north of it might influence the onset of the African monsoon through the intensification of the southerly winds in the Gulf of Guinea [*Okumura and Xie*, 2004]. SST is thought to have a strong impact on the meridional gradient of moist static energy in the atmospheric boundary layer between the Gulf of Guinea (GG) and the continent, and the GG provides 20% of the water vapor to the African Monsoon flux [*Fontaine et al.*, 2003].

[3] Many studies of the annual cycle of the ocean vertical structure in the tropical Atlantic, with observations [*Houghton*, 1991] and with models [*Busalacchi and Picaut*, 1983; *Du Penhoat and Treguier*, 1985; *Philander and Pacanowski*, 1986] have shown that the annual cycle of the thermocline (generally represented by the variability of the 20°C isotherm depth, referred to hereafter as D20) is controlled by wind forcing on the basin scale. Following the intensification of the trade winds, the currents increase and the thermocline shoals in the eastern part of the basin [*Houghton*, 1989], which results in the formation of a cold tongue in the equatorial upwelling region with colder water closer to the surface.

[4] The seasonal evolution and maintenance of the cold tongue also depend on dynamic processes, such as vertical and horizontal advection, vertical mixing, and heat flux

[1]Laboratoire d'Etudes en Géophysique et Océanographie Spatiales, Centre National d'Etudes Spatiales, CNRS, Institut de Recherche Pour le Développement, Université Paul Sabatier, Toulouse, France.
[2]Laboratoire d'Océanographie et du Climat: Expérimentation et Approches Numériques, CNRS, Université Pierre et Marie Curie, Institut de Recherche Pour le Développement, Museum National d'Histoire Naturelle, Paris, France.
[3]Centre National Recherche Météorologique, Toulouse, France.

0148-0227/06/2005JC003157

divergence associated with Tropical Instability Waves (TIWs), which are common to the Pacific and Atlantic oceans.

[5] In the equatorial Atlantic Ocean, a number of observational studies [e.g., *Merle*, 1980] and modeling studies [*Philander and Pacanowski*, 1986] have addressed the causes of the annual cycle of SST. They found intense warming by atmospheric heat fluxes, for both the mean balance and the seasonal cycle. The vertical processes (vertical advection, mixing, and entrainment) are the main cooling terms balancing the warming by atmospheric fluxes, but horizontal advection is also a significant contributor. *Foltz et al.* [2003] (hereinafter referred to as FGCM) used a variety of satellite and in situ data sources (data from Pilot Research Moored Array in the Tropical Atlantic (PIRATA) moorings) to examine the causes of the seasonal cycle of SST in response to seasonally varying surface heating and winds, in the tropical Atlantic Ocean, through a heat budget analysis. They characterized three different equatorial regions (corresponding to the location of three equatorial moorings): (1) the western part of the basin near 35°W in which the seasonal cycles of zonal heat advection, eddy advection, entrainment and net surface heat flux all contribute significantly to the seasonal SST variability, (2) the central equatorial region (23°W), with a similar heat balance except that seasonal variations of latent heat and entrainment cooling are significantly smaller, and (3) the eastern equatorial region (10°W) where cooling from mean meridional advection and warming from eddy advection tend to balance so that SST seasonal changes are mainly driven by absorbed shortwave radiation.

[6] However, the observational studies cannot evaluate explicitly every term of heat budget, in particular the vertical terms that are very difficult to compute directly. These studies are also subject to sampling error because of the insufficient temporal and spatial resolution. This is especially true for the heat transported by TIWs that requires high-resolution data sets to be resolved satisfactorily [*Jochum et al.*, 2005]. By using a model, a complete and consistent picture of the ocean circulation is given. This allows a precise evaluation of all contributions to a closed heat budget. In this study, the OPA-CLIPPER [*Treguier et al.*, 2001] Ocean Global Circulation Model (OGCM) is used to assess the role of the different oceanic processes in the tropical Atlantic heat budget and to determine the mechanisms responsible for the SST mean balance and seasonal cycle. The model characteristics, the mixed layer heat budget equation, and the data sets used for the validation are introduced in section 2. In sections 3 and 4, the ocean state is described and validated, and the heat budget is analyzed, respectively for the mean state and the seasonal cycle. Results are then discussed in section 5 and summarized in section 6.

2. Model and Methodology

2.1. Modeling Approach

[7] The ocean model used in this study is the primitive equation OGCM OPA 8.1 [*Madec et al.*, 1998] in the CLIPPER configuration [*Treguier et al.*, 2001; *Arhan et al.*, 2006]. This configuration uses z coordinates on the vertical (42 geopotential vertical levels with 12 levels in the first 200 m). It covers the Atlantic Ocean from the Drake Passage to 30°E and from Antarctica (75°S) to 70°N, with a Mercator isotropic grid at 1/6° resolution at the equator. There are four open boundaries, at Drake Passage, at 30°E between Africa and Antarctica, in the Gulf of Cadiza and at 70°N in the Nordic seas [*Treguier et al.*, 2001].

[8] A horizontal biharmonic operator is used for lateral mixing of momentum with a coefficient of 5.5 10^{10} m^4 s^{-1} at the equator, varying with the third power of the grid spacing. Mixing of temperature and salinity is done along isopycnals using a Laplacian operator, with a coefficient of 150 m^2 s^{-1} at the equator, also varying in latitude with the grid spacing. The vertical mixing of momentum and tracers is calculated using a second-order closure model [*Madec et al.*, 1998]. In case of static instability, the vertical mixing coefficients are set to the large value of 1 m^2 s^{-1}. An enhanced Laplacian mixing of momentum is added in the upper equatorial band so as to prevent the Equatorial Under Current (EUC) from being too intense [*Michel and Treguier*, 2002]. The added Laplacian diffusion of momentum has a constant coefficient 10^3 m^2 s^{-1} between 1°N and 1°S and above 60 m, decaying to zero at 3° of latitude and 120 m depth. This additional mixing term accounts for inertial instability processes that are not present in the model, at this spatial resolution [*Richards and Edwards*, 2003].

[9] All surface forcing fields apart from the wind stress are derived from the European Centre for Medium-Range Weather Forecasts (ECMWF) Re-Analysis ERA-15 for the period covering 1990 to 1993 [*Gibson et al.*, 1997], and from the ECMWF analysis for the years 1994 to 2000. The non solar heat fluxes are formulated as suggested in *Barnier et al.* [1995], using a relaxation to the observed SST [*Reynolds and Smith*, 1994], with a feedback coefficient taken equal to -40 W m^{-2} K^{-1}, which corresponds to a relaxation timescale of 2 months for a 50 m mixed layer depth. A relaxation to a climatological sea surface salinity with a similar timescale is added to the evaporation minus precipitation fluxes which are formulated as a pseudo salt flux, and include a river runoff [*Treguier et al.*, 2001]. The wind stress forcing is derived from Earth Remote Sensing (ERS)1–2 wind scatterometers (http://www.ifremer.fr/cersat/) [*Grima et al.*, 1999]. ERS winds were chosen instead of ECMWF because of the higher-quality wind forcing, especially in the eastern part of the basin (A. M. Treguier, personal communication, 2004).

[10] A 3 year spin-up procedure is used as follows: The model is run from 1990 to 1992 using heat and salt fluxes from ECMWF, and the climatology of ERS wind stress obtained by averaging years 1993 to 2000. Then, the model is forced by weekly ERS wind stress data between 1993 and 2000, and by daily ECMWF fluxes. More attention was paid to the heat budget in the equatorial basin for the years 1997 to 2000 away from the coastal regions (the model is not able to reproduce these particular dynamics, which are beyond the scope of the present study).

2.2. Mixed Layer Heat Budget

[11] This approach has already been used, for example, to investigate the SST balance in the tropical Pacific Ocean on seasonal to interannual timescales [*Vialard et al.*, 2001] and the contributions to intraseasonal SST variability in the Indian Ocean [*Duvel et al.*, 2004]. In the present study,

the mixed layer temperature equation is decomposed as described by *Menkes et al.* [2006]:

$$\partial_t\langle T\rangle = \underbrace{\left\langle -\overline{u}.\partial_x\overline{T}\right\rangle}_{a} + \underbrace{\left\langle -\overline{v}.\partial_y\overline{T}\right\rangle}_{b} - \underbrace{\left\langle \overline{u'\partial_x T'}\right\rangle - \left\langle \overline{v'\partial_y T'}\right\rangle + \langle D_l\rangle}_{c} \underbrace{- \frac{(K_z\partial_z T)_{(z=-h)}}{h} - \frac{1}{h}\left(\partial_t h + w_{(z=-h)}\right)\left(\langle T\rangle - T_{(z=-h)}\right)}_{d} + \underbrace{\frac{Q^* + Q_s\left(1 - f_{(z=-h)}\right)}{\rho_0 C_p h}}_{e} + \underbrace{\langle (T - \langle T\rangle)\partial_z w\rangle}_{res} \quad (1)$$

with

$$\langle \bullet\rangle = \frac{1}{h}\int_{-h}^{0} \bullet dz$$

[12] Here, T is the temperature; u, v and w are respectively the zonal, meridional and vertical currents, K_z the vertical mixing coefficient for tracers, h the Mixed Layer Depth (MLD), and D_l the lateral diffusion. The last term (e) on the right hand side corresponds to the atmospheric forcing, Q^* and Q_s are the nonsolar and solar components of the total heat flux, and f ($z = -h$) is the fraction of the solar shortwave that reaches the mixed layer depth h. A formulation including extinction coefficients (0.35 m and 23 m) is assumed for the downward irradiance [*Paulson and Simpson*, 1977]. Note that the flux term contains a damping term, proportional to the difference between the modeled and the observed SST from *Reynolds and Smith* [1994]. The MLD is defined as the depth at which the density is equal to surface density plus 0.05 kg m^{-3}. The $\langle . \rangle$ represent a quantity integrated over the mixed layer.

[13] To separate low- and high-frequency horizontal advections, the 35-day Hanning-filtered low-frequency component of currents and temperature (denoted by overbars) are first computed offline, and are then integrated over the Mixed Layer (ML) (terms a and b in equation (1)). Higher-frequency advection (first two terms of (c) in equation (1)) is then deduced by subtracting the previously computed low-frequency advection from the total horizontal advection. It was checked that the result depended only slightly on the chosen period for the filter.

[14] This decomposition allows the five terms contributing to SST evolution to be isolated. The temperature evolution, defined as heat storage, is governed by the sum of the zonal advection by (1) low-frequency currents, (2) meridional advection by low-frequency currents, (3) effect of eddies for periods of less than 35 days (the usually small lateral diffusion is also included in this term), (4) subsurface effects (grouping turbulent mixing, entrainment, computed as a residual in the routine which vertically averages the different terms in the ML, and vertical advection), (5), atmospheric forcing, and (6) a residue (res) which was checked to be negligible (three orders smaller than the others terms) because the temperature is very close to its mean in the mixed layer. This residue will not be considered hereafter. In the tropical Atlantic, the so-called ''eddies'' include Brazil Current eddies, TIWs and intraseasonal equatorial wave activity. However, TIWs are the main contributors to this eddy term, in agreement with a study in the Pacific [*Menkes et al.*, 2006]. The dominant contributor to the subsurface term proves to be the vertical diffusion at the base of the mixed layer, with a minor role for upwelling. This is due to our computation of the heat budget over a time and space varying mixed layer. This contrasts with a heat budget calculated over a constant depth mixed layer in which vertical advection dominates vertical diffusion.

2.3. Validation

[15] In order to validate the MLD, thermocline depth, temperature vertical structure, Sea Level Anomalies (SLA) and currents in the model, different observation data sets were used. TOPEX/Poseidon-ERS (T/P-ERS) SLA are used, on a 1/4° × 1/4° grid every 10 days. The SLA were built after removing the mean sea surface over 7 years (1993–1999) [*Le Traon et al.*, 1998]. The accuracy of this product is about 2–3 cm RMS in the Tropics. The PIRATA moored buoy array [*Servain et al.*, 1998] consist of ten moorings which measure subsurface temperatures at 11 depths between 1 and 500 m with 20 m spacing in the upper 140 m. The Tropical Atlantic Ocean Subsurface Temperature Atlas (TAOSTA) is an interannual database of vertical temperatures (0–500 m) between 1979 and 1999, over a domain extending from 70°W to 12°E and 30°S to 30°N, with a 2° × 2° latitude-longitude grid [*Vauclair and Du Penhoat*, 2001]. Modeled MLD are validated using the global mixed layer depth climatology from *de Boyer Montégut et al.* [2004] (hereinafter referred to as dBM) available on a 2° × 2° spatial grid at a monthly resolution, and computed from the same density criterion as in CLIPPER. SST weekly mean maps from the TRMM Microwave Imager (TMI; see www.remss.com) radiometer between 1998 and 2000, at a resolution of 0.25° are also used. Finally, *Richardson and McKee* [1984] (hereinafter referred to as RMK) provide a monthly climatology of ship drift–derived surface currents on a 1° × 1° grid within the region 20°S–20°N, 10°E–70°W.

[16] The SLA spatial variability from the model is comparable to T/P-ERS (Figure 1). Both low- and high-variability regions are well located with comparable amplitude. However, there is a lack of variability in the CLIPPER experiment in the northwestern part of the basin, especially in the retroflection region (10 cm for T/P and 8 cm for the model; see Figures 1a and 1b). This also corresponds to the lowest correlation and highest RMS differences (Figures 1c and 1d).

[17] The vertical structure (temperature and D20) in the model is in reasonable agreement with PIRATA temperature measurements (Figure 2) despite an underestimation of high-frequency variability in the thermocline in the model. Moreover, the model is too cold near the surface, especially at 23°W where differences between the model and observations reach up to 1°C. Finally, the thermocline is too diffuse compared to observations, a common flaw of numerical models in the equatorial regions.

3. Mean State

3.1. Description and Validation

[18] The Tropical Atlantic is subject to a trade wind regime whose seasonal variations partly govern the ocean.

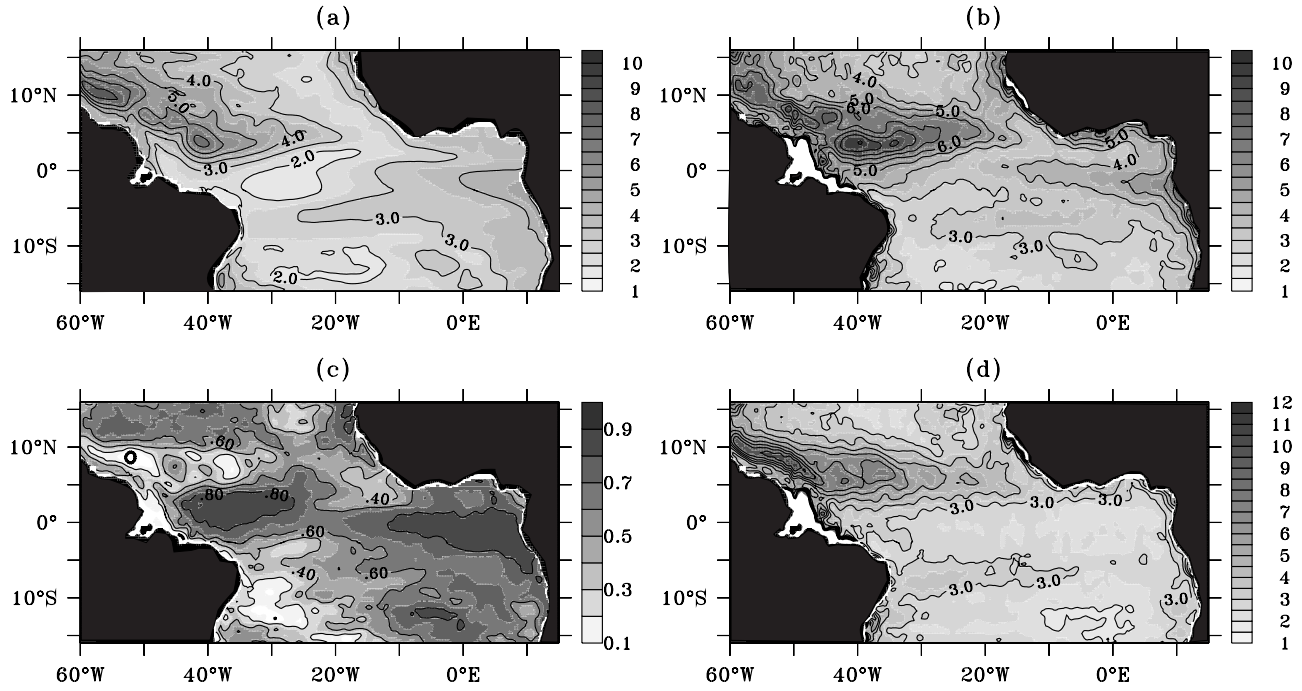

Figure 1. Longitude-latitude plots of CLIPPER and T/P-ERS sea level anomalies: (a) CLIPPER standard deviation, (b) T/P standard deviation, (c) correlation, and (d) RMS difference (contours every 1 cm, except for correlation, whose contour interval is 1). For this comparison we have linearly interpolated the model on the T/P-ERS grid.

The south east and north east trade winds converge in the ITCZ whose position in the northern hemisphere is one factor which explains the presence of cold water just south of the equator, and warmer water north of it [see, e.g., *Mitchell and Wallace*, 1992]. The net heat flux is maximum above the cold tongue (160 W m^{-2}), and minimum over the subtropical gyres (Figure 3a). The ECMWF global structure is in good agreement with other atmospheric heat flux data set. However, the zonally averaged net flux along the equator from ECMWF (37 W m^{-2}) is underestimated when compared to other data sets which are anyway not consistent together (for instance, 47 W m^{-2} for NCEP/NCAR Reanalysis; 60 W m^{-2} for UWM/COADS, and 89 W m^{-2} for SOC; for more details, see http://www-meom.hmg.inpg.fr/Web/Atlas/Flux/main.html). This is mainly due to too weak solar and latent heat fluxes [*Yu et al.*, 2004].

[19] The modeled mean circulation in the upper ocean is realistic (Figure 3b), with the two branches of the westward flowing South Equatorial Current (SEC) off the equator, separating into the southward flowing Brazil Current and the northward flowing North Brazil Current. The latter feeds the Guyana Current, and the eastward North Equatorial Countercurrent (NECC) which extends into the Guinea Current in the GG. The subsurface circulation is validated and discussed in a specific study about the EUC [*Arhan et al.*, 2006].

[20] The modeled spatial D20 distribution is in agreement with TAOSTA observations [*Vauclair and Du Penhoat*, 2001] (Figures 4a and 4b). The zonal and meridional slopes of the thermocline are similar in the model and the data: along the equator, the thermocline deepens from 50 m in the east to 120 m in the west in both data and model.

[21] Figures 4c and 4d depict the mean mixed layer depth, in comparison with the dBM's mixed layer depth climatology. The MLD is shallower in the eastern part of the basin: 10 m (both model and data), and deepens toward the west reaching 60 m in the observations but only 40 m in the model. This underestimation of the MLD is due to the combined effects of the absence of the very high-frequency wind stress forcing and of the insufficient vertical resolution which prevents the transmission of the wind stress energy to the current shear and thus prevents the MLD from deepening [*Blanke and Delecluse*, 1993]. Note that the high spatial resolution of the model allows the narrowness of the shallow mixed layer in the equatorial band to be reproduced. This is not visible with a weaker resolution such as in the work by dBM, but it is confirmed by close examination of vertical profiles from hydrographic cruises such as EQUALANT [*Bourlès et al.*, 2002]. Despite a slight underestimation of the modeled MLD in the west, the model demonstrates a good ability to reproduce the mixed layer depth structure, a key feature for mixed layer heat budgets.

3.2. Heat Budget

[22] Figure 5 shows the mean 1997–2000 state of the different tendency terms of equation (1). Over that time period, heat storage (left-hand side of equation (1)) is observed to be close to zero.

[23] The overall balance mainly results from cooling by vertical processes at the base of the ML (vertical advection, entrainment, vertical mixing), warming by atmospheric heat fluxes, and eddies, a picture very similar to *Vialard et al.*'s [2001] and *Menkes et al.*'s [2006] results in the Pacific Ocean. The subsurface cooling is greater than 2.5°C

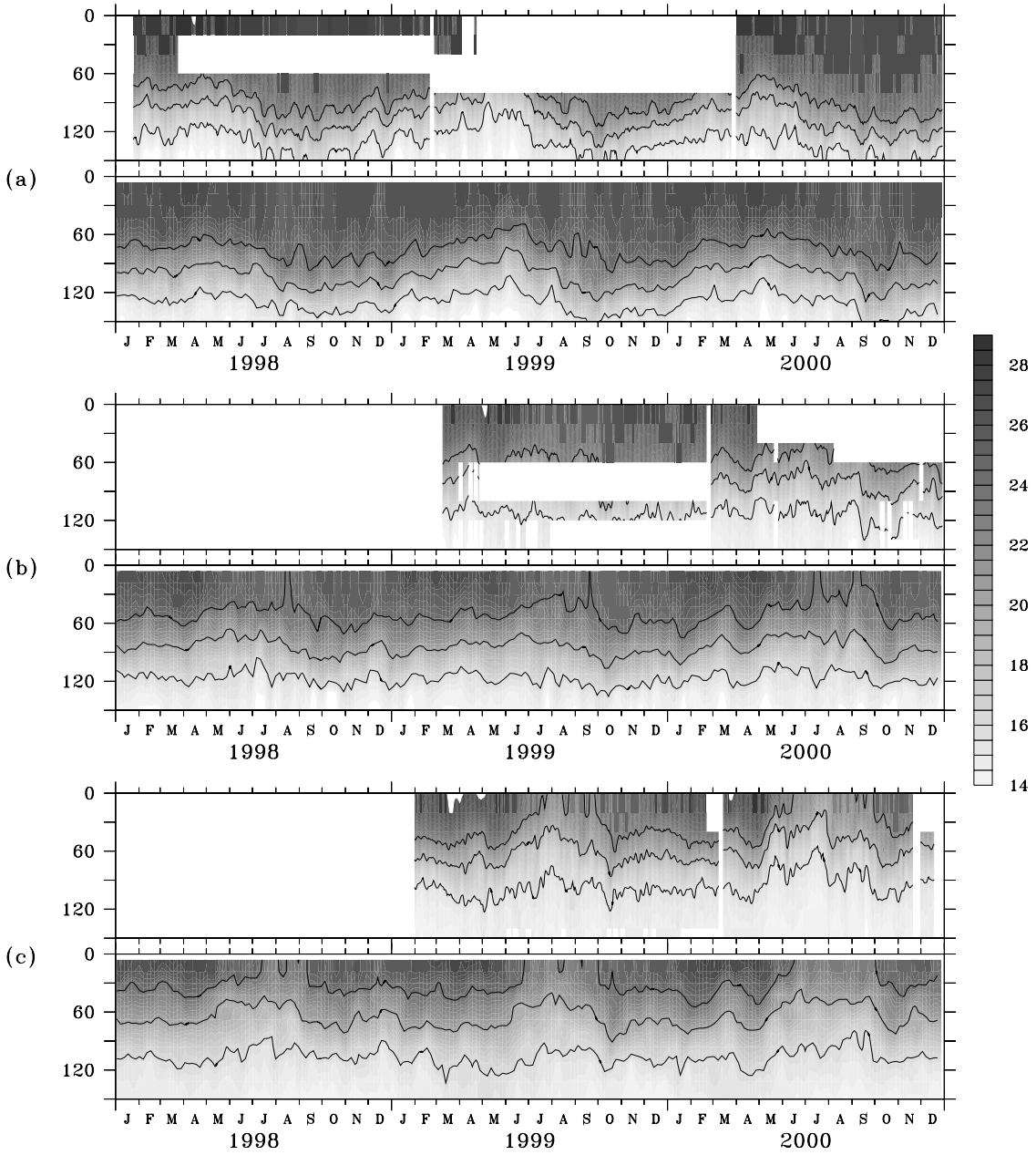

Figure 2. Time-depth plots of (top) PIRATA moorings and (bottom) model temperature along the equator at various longitudes: (a) 35°W, (b) 23°W, and (c) 10°W (contours are 16°C, 20°C, and 24°C). The PIRATA data are filtered (5-day filtered).

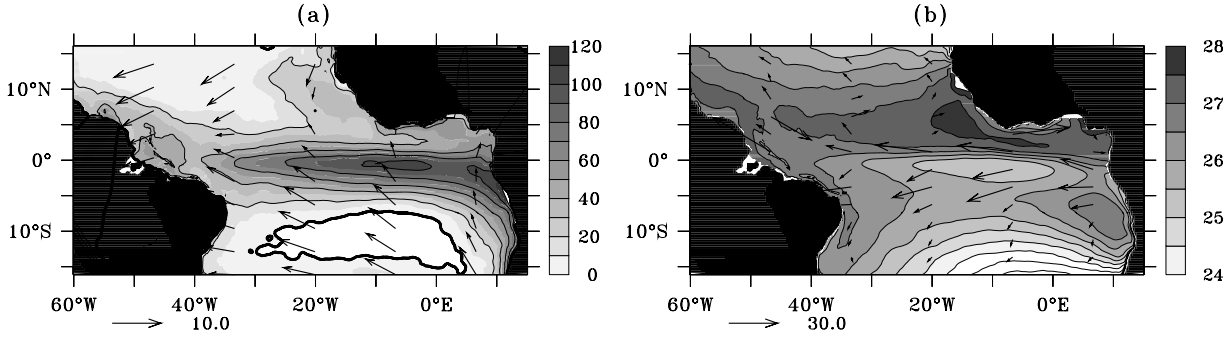

Figure 3. Longitude-latitude plots of the 1997–2000 time average of (a) ECMWF total heat flux (contours every 20 W m^{-2}) and ERS wind stress (10^2 N m^{-2}) and (b) CLIPPER mixed layer temperature (contours every 0.5°C) and CLIPPER currents (cm s^{-1}).

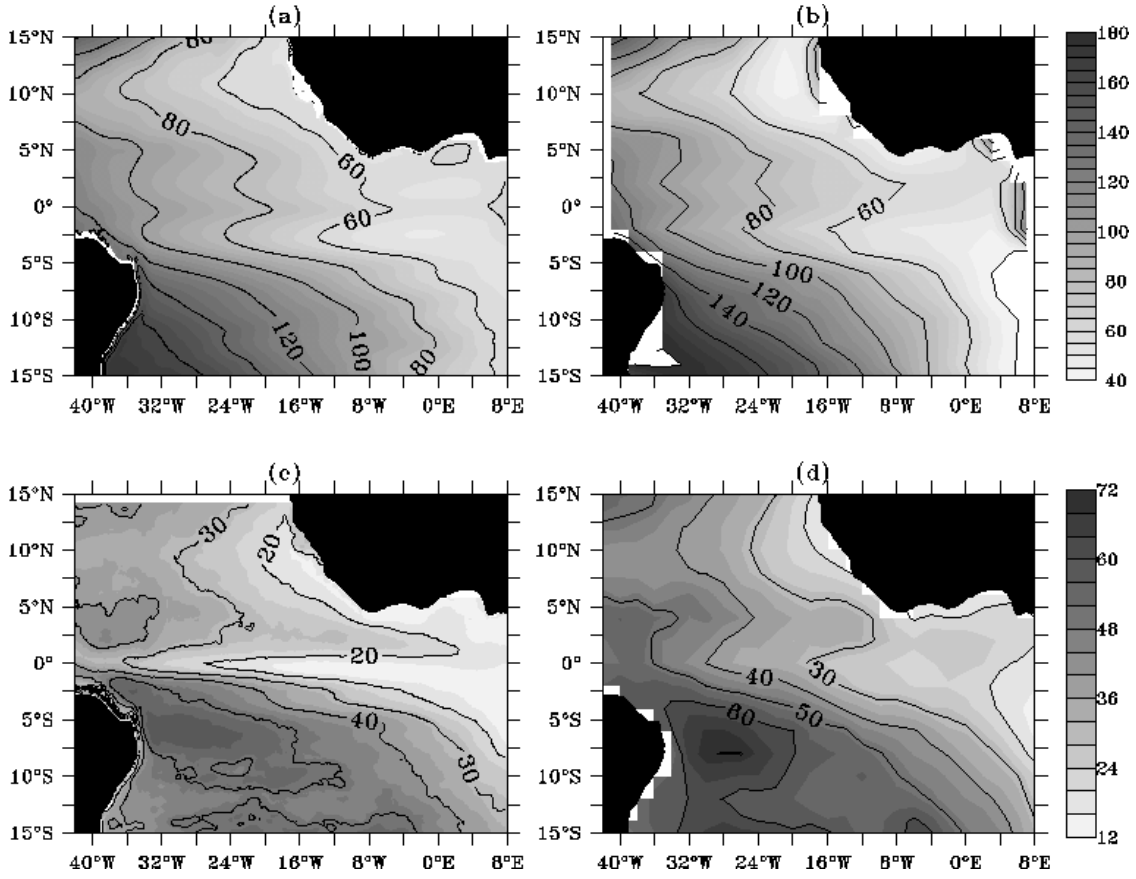

Figure 4. Longitude-latitude plots of the 1997–2000 time average of the 20°C isotherm depth for (a) CLIPPER and (b) TAOSTA (contours every 20 m) and of the mixed layer depth for (c) CLIPPER and (d) *de Boyer Montégut et al.* [2004] (contours every 10 m). The criterion for the MLD is the depth at which the density equals the surface density plus 0.05 kg m^{-3}.

month^{-1} south of the equator (0°S–2°S), from 0°W to 20°W. Over the same area, warming by the atmospheric fluxes is about 1.5 to 2°C month^{-1}. Warming by eddies contribute to a rate of 1 to 1.5°C month^{-1} between 5°W and 30°W slightly north of the equator. The mean low-frequency meridional advection plays a minor role in the overall balance and has mainly a cooling effect north of the equator (0°N–2°N) between 0° and 25°W, with values locally reaching 1°C month^{-1}. Finally, low-frequency zonal advection is a minor term only contributing to a warming patch of 0.5°C month^{-1} north of the equator (0°N–2°N) in the western part of the GG (0° and 10°W).

[24] The atmospheric forcing term largely reflects the structure of the atmospheric net heat fluxes (Figures 5a and 3a). Its pattern is close to the total net heat flux, but depends also on the spatial structure of the mean MLD (Figure 4c). A shallow MLD indeed concentrates the net heat flux and increases the warming tendency close to the equator. The strongest heating thus also corresponds to the region of the strongest upwelling, enhancing the moderating effect of the atmospheric fluxes on the equatorial upwelling.

[25] The mean subsurface tendency term (Figure 5b) is a cooling term all over the equatorial band. Like the atmospheric warming, the subsurface cooling is also the strongest in the equatorial cold tongue: first, this is a region of Ekman divergence and upwelling, with a thin thermocline and a strong vertical temperature gradient; secondly, the strong vertical shear between the surface SEC and the EUC results in strong vertical mixing.

[26] The warming by the eddy term is located in the region of most active TIWs [*Chelton et al.*, 2000], and is similar in magnitude to the seasonal atmospheric heat flux. The TIWs are tightly trapped within a narrow band north of the equator, and reach their maximum at 15°W, in agreement with satellite observations [*Legeckis and Reverdin*, 1987; *Caltabiano et al.*, 2005]. In agreement with *Jochum et al.* [2004], the lateral diffusion is observed to be negligible when compared to TIWs.

[27] The low-frequency zonal advection heating pattern on the equator between 10°W and 0° is due to the westward current that brings warmer waters from the east of the cold tongue (Figure 3b). Like the zonal advection, the mean advection by low-frequency meridional currents (Figure 4e) does not play a major role in the total balance. North and south of the cold tongue the meridional current flows poleward, in response to the equatorial divergence and thus brings colder water: this is a cooling term. This cooling is less effective in the south as the

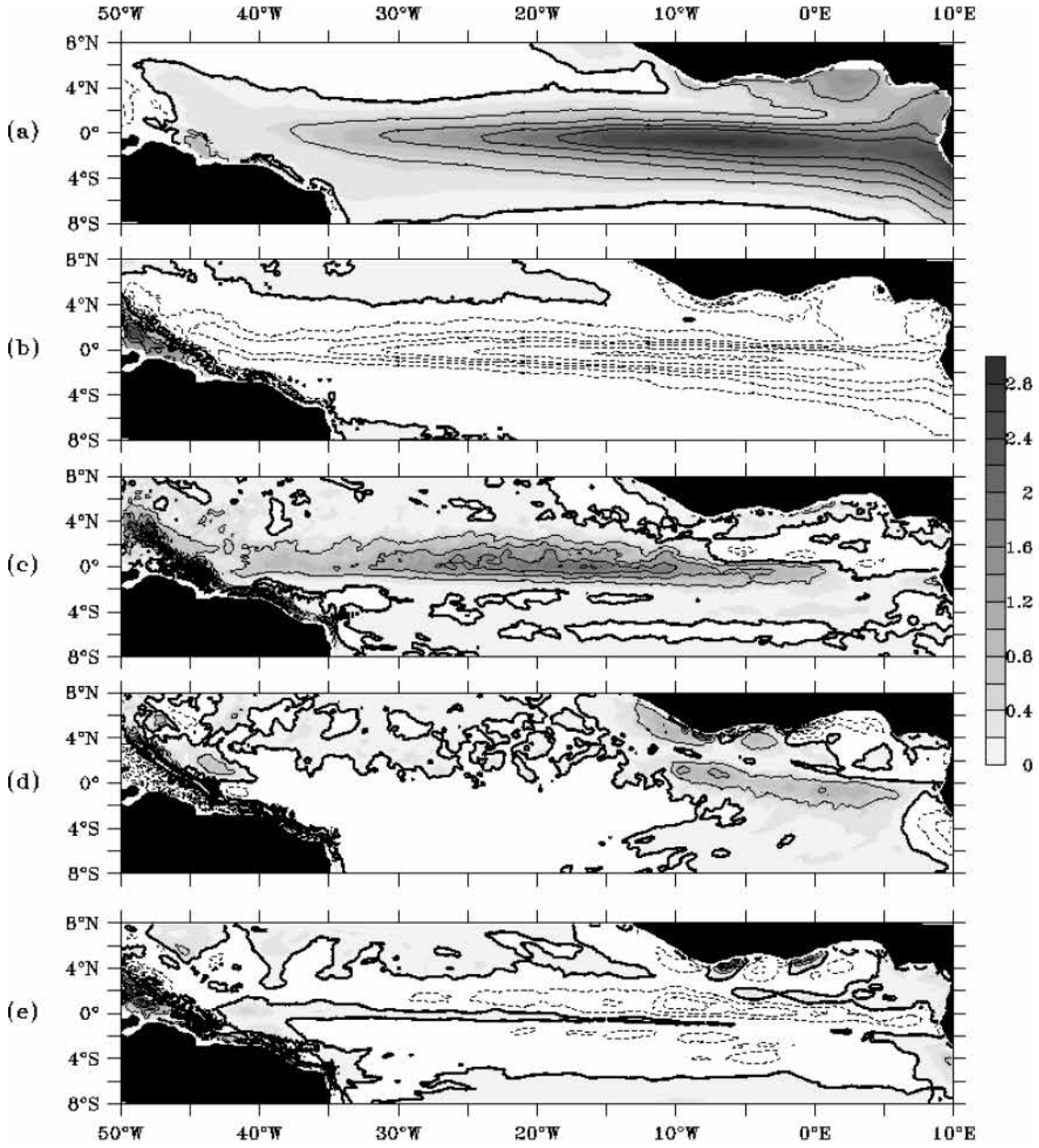

Figure 5. Longitude-latitude plots of the 1997–2000 time average of various contributors to the mixed layer temperature: (a) atmospheric forcing, (b) tendencies due to vertical exchanges with the subsurface ocean (sum of vertical advection, vertical diffusion at the base of the mixed layer, and entrainment), (c) eddies (high-frequency horizontal advection plus lateral diffusion), (d) zonal advection by low-frequency currents, (e) meridional advection by low-frequency currents (contours every 0.5°C month^{-1} between −2°C month^{-1} and 2°C month^{-1} and every 1°C month^{-1} after; the thick line is zero; and dashed contours represent negative values).

meridional temperature gradient is weaker than in the north.

4. Seasonal Cycle

4.1. Description and Validation

[28] Figure 6 shows the seasonal cycle of zonal wind stress, net heat flux and thermocline depth. In March, the net flux (Figure 6a) reaches its first maximum in the central part of the basin (110 W m^{-2}), when wind stresses are low (0.04 N m^{-2}). From March to May the net heat flux decreases along the equator while zonal wind stress and latent heat flux increase, driving the net heat loss close to its minimum in May (∼20 W m^{-2}). The wind in the eastern part of the GG blows eastward in the GG (monsoon flux), and strengthens between August and October. The net heat flux thus reaches its second maximum in late September (120 W m^{-2}). From September to December, the net heat flux decreases to a second minimum (60 W m^{-2}). These features are in agreement with *Chang et al.* [2000]. Figure 6c shows the seasonal cycle of the modeled thermocline

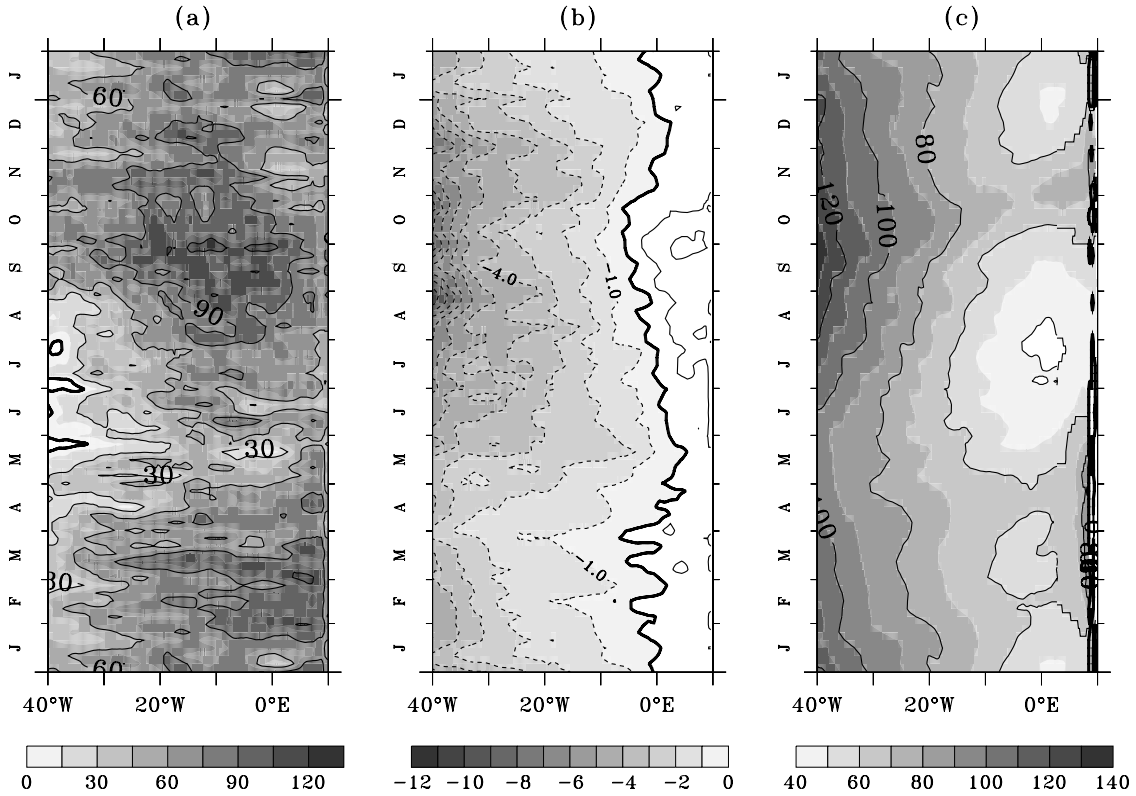

Figure 6. Longitude-time plots along the equator (2°N–2°S average) for the mean 1997–2000 seasonal cycle of (a) ECMWF net heat flux (contours every 30 W m^{-2}), (b) ERS zonal wind stress (contours every 10^{-2} N m^{-1}), and (c) model 20°C isotherm depth (contours every 20 m).

depth which tightly responds to wind-forcing variability (Figure 6b). In March the east-west thermocline slope is slightly tilted and reverses east of 5°W; this slope starts to increase in May and June during the intensification of the easterlies. As the easterlies relax in the center of the basin between June and October, the thermocline deepens at 0°E. The second intensification of the trade winds in November makes the thermocline shallow again in the whole basin. These features are in good agreement with *Hastenrath and Merle* [1987].

[29] Figures 7a and 7b represent the SST seasonal cycle, from the model and TMI. In March–April, the SST reaches its maximum (28.5°C in the model, 29.5°C for TMI) in the eastern part of the basin. Then the SST drops until August (23.5°C in the model and 23°C in observations) when the trade winds are strongest. Then, SST slowly rises from August to March, except in boreal winter in the GG with a short cold season in the model. This secondary cooling is generally not captured well in most widely used climatological data because of their low resolution in space and time. However, the 6-year PIRATA buoy observations support the existence of this secondary seasonal cooling (not shown). Notice that the seasonal warming and cooling are highly asymmetric at 10°W, with the latter taking only 3 months and the former taking 7 months. From the oceanic point of view, this rapid cooling can be attributed to the sudden and rapid intensification of the southerly winds in May–June in the GG, in link with the West African monsoon [*Li and Philander*, 1997; *Xie and Carton*, 2004]. The main features of the SST seasonal cycle are well captured by the model, despite a lack of amplitude compared to TMI, in particular the cold tongue is not cold enough in boreal summer.

[30] Figure 7c depicts the seasonal variations of the model MLD in comparison with dBM's climatology (Figure 7d). As the winds are more intense in the west, the mixed layer is deeper there than in the east. In March–April, the wind stress is very weak and the ocean remains highly stratified: the mixed layer is shallow (12 m from the African coast to 30°W in the model but deeper in the observations). During May and June, the sudden increase of the easterly wind stresses very rapidly deepens the mixed layer in both model and observations. When wind stress relaxes after November, the mixing reduces, the top of the ocean stratifies and the ML thins. The MLD variations are around 30 m in the west and 10 m in the east, representing a variation of 100% over the course of the season. Notice that, even though the seasonal cycles of the thermocline and the mixed layer depths are similar in the central and western tropical Atlantic, the cycles are not in phase in the east: when the MLD rapidly varies, the thermocline depth is at an extremum, and vice versa (i.e., ∂_tMLD maximum when ∂_tD20 = 0, and ∂_tD20 maximum when ∂_tMLD = 0).

[31] The seasonal cycles of the zonal current along the equator, for the simulation and the RMK product, are shown in Figures 7e and 7f. In April, the westward flowing SEC strengthens with the intensification of the trade winds (Figure 6b), and reaches its maximum in June (0.5 m s^{-1}) with the right timing and location compared to RMK, although with a weaker than observed intensity. During

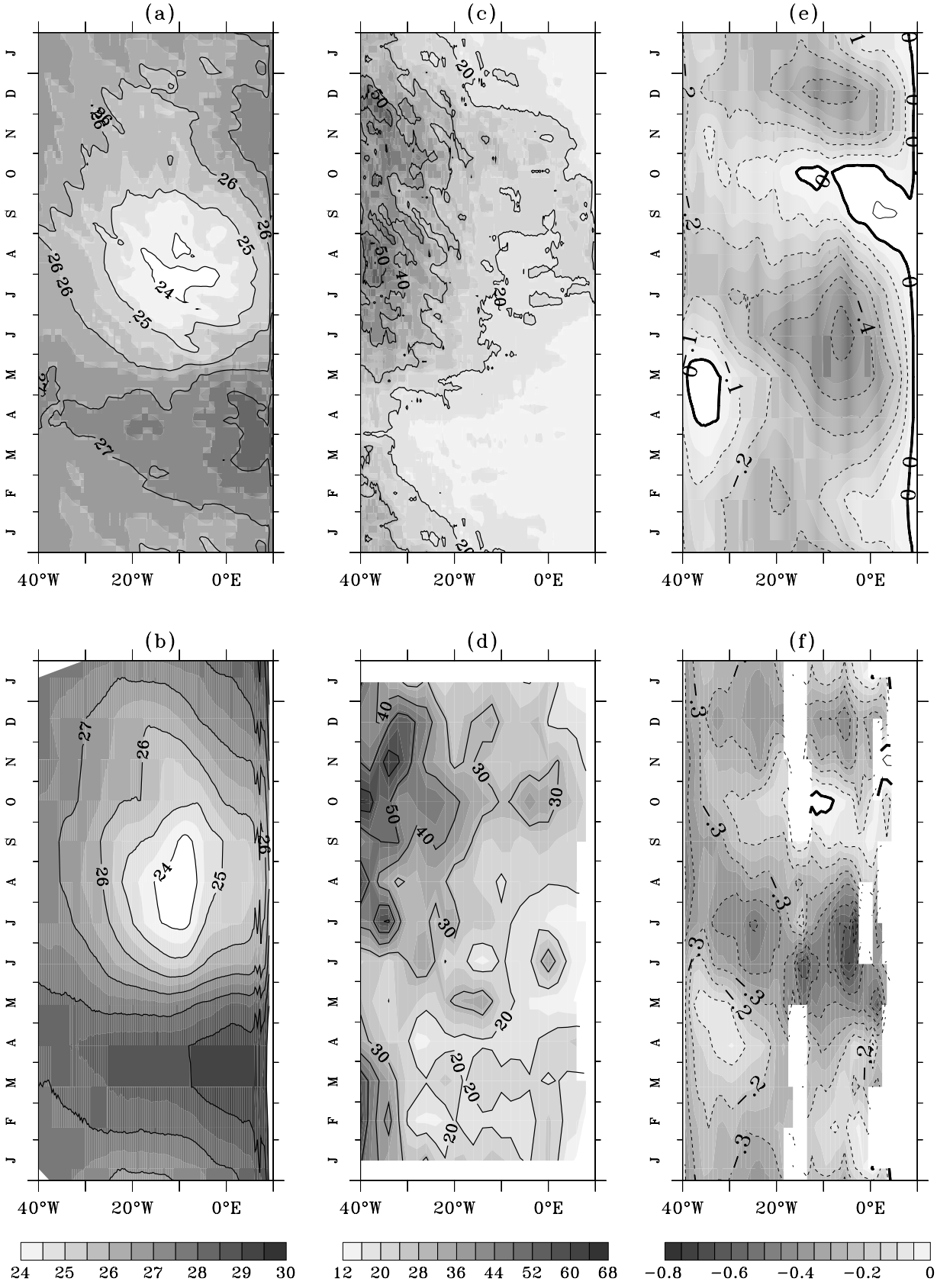

Figure 7. Same as Figure 6 but for SST from (a) CLIPPER and (b) TMI (contours every 1°C), MLD from (c) CLIPPER and (d) *de Boyer Montégut et al.* [2004] (contours every 10 m), and zonal current from (e) CLIPPER and (f) *Richardson and McKee* [1984] (contours every 0.1 cm s^{-1}). The data of *Richardson and McKee* [1984] are smoothed (1° longitude Hanning filter).

the relaxation of the easterlies and the strengthening of the westerlies (Figure 6b), the SEC drops and reverses from the GG to 15°W in September and October in agreement with RMK and other studies [*Weisberg and Weingartner*, 1988]. The second intensification of the trade winds in November (Figure 6b) is associated with a second strengthening of the SEC that reaches a maximum (0.4 m s^{-1}) in both model and data.

4.2. Seasonal Heat Budget

4.2.1. Along the Equator

[32] This section first describes the heat balance in the equatorial band (2°N–2°S mean). The various tendency terms of the heat budget seasonal cycle (1997–2000 mean) are presented in Figure 8.

[33] Heat storage along the equator is driven by the cooling action of the subsurface term (Figure 8c), and the warming by both atmospheric forcing (Figure 8b) and eddies (Figure 8d). Zonal and meridional advections by low-frequency currents are relatively weak except in boreal summer (Figure 8e), and compensate each other. For more legibility, they are regrouped. There are four distinct periods in the heat storage seasonal cycle (Figure 8a): (1) from January to the end of March, the mixed layer warms slowly, (2) in April, the cooling starts, and goes on until August, with a maximum cooling in May of around 5°W, (3) the mixed layer is then heated again until December, (4) in December, a second and weaker boreal winter cooling can be identified in the eastern part of the basin (Figure 7a).

[34] Between January and March, as the ITCZ moves close to the equator, winds and currents are weak (Figures 6b and 7e); the contributions of the subsurface cooling term and the TIWs are thus weak, and the surface heating is the dominant term (Figure 8b) that drives the positive heat storage and the resulting SST warming with a maximum SST at the end of March (Figure 7a).

[35] The strong cooling between April and August is linked to both a clear decrease in the warming by atmospheric forcing and an increase in the subsurface cooling, but is moderated by warming by TIWs. In April and May, the easterlies suddenly strengthen at the equator, forcing a strong SEC (Figures 6b and 7e). Atmospheric heat forcing drops (Figure 6a) because of the decrease in solar heat flux and the increase in latent heat loss via evaporative cooling. Vertical diffusion cooling, induced by strong mixing processes, is enhanced. At that time, the currents are swift and are prone to instability; they generate tropical instability waves in the center of the basin, that act to warm the equatorial band from 5°W to 30°W (Figure 8d). This warming by TIWs is not strong enough to counteract the two previous effects, which result in a net heat loss and a progressive SST decrease, reaching its minimum at the beginning of August (Figure 7a). In the far western part of the basin, the increase in latent heat loss is enhanced by higher wind stress (Figure 6b), the subsurface cooling is less efficient as the thermocline remains deep, and the warming by the TIWs remains weak because the waves generated around 5°W have not yet reached the western part of the basin; almost every term plays a role in the SST drop there. East of 15°W, TIWs play almost no role and vertical diffusion cooling induced by strong mixing processes dominates over all terms.

[36] From August to November, atmospheric forcing significantly increases again (Figure 8b) because of higher solar heat flux and weaker easterlies in the center of the basin (Figure 6b). In association with the wind decrease, the drop in westward currents (Figure 7e), stratification (Figure 6c) and shears (horizontal and vertical) in September and October reduce the effects of both subsurface cooling and warming by TIWs. The situation is quite different in the far western part of the basin where the easterlies (and the SEC) increase in July and August (Figures 6b and 7e). This leads to an increase in subsurface cooling compared to the previous period, due to stronger mixing at the base of the ML. The TIWs also remain intense there. The warming by eddies and the subsurface cooling partly compensate each other and the increase in surface net heat flux drives the observed rise of the SST. In the GG, the TIWs are almost nonexistent, so the heat storage is dominated by the surface warming and the subsurface cooling. The atmospheric forcing is weak from August to November, as the westward current decreases and even reverses in the GG. The decrease in stratification and in subsurface cooling, together with the increase of surface atmospheric forcing, leads to a warming of the sea surface (Figure 8a). Though partly balanced by the subsurface term and modulated by TIWs in the western part of the basin, the increase in solar radiation is the dominant factor that explains the warming from August to November (Figure 7a).

[37] In boreal fall and winter, the atmospheric warming decreases in the GG during the winter monsoon because of the associated high cloud coverage [*Okumura and Xie*, 2005]. Only in the GG the decrease in solar flux, associated with the increase in subsurface cooling, allows the SST to cool.

[38] The overall analysis explains why the SST seasonal cycle is annual in the central and western parts of the basin, with a short intense cooling period between April and July and a longer period of slight warming, and semiannual in the GG with a short second cooling period in December.

4.2.2. Latitudinal Structure

[39] To characterize latitudinal structure of the heat budget, two longitudes were selected: 23°W (representative of western and central parts of the basin and location of PIRATA moorings) and 3°E (eastern part of the basin and location of repeated hydrographic sections).

[40] At a first glance, Figure 9 shows that the heat storage evolution south of the equator and north of it is mainly governed by atmospheric forcing in the central part of the basin (Figures 9a and 9b). North (4°N–8°N) and south (4°S–8°S) of the equator, the subsurface term tends to cool the mixed layer temperature except during the cold season when it tends to warm it at 23°W because of the presence of a barrier layer. Except in the northeastern part of the basin where the eddies play a significant role in the temperature evolution (Figure 9c), this term is very small, like low-frequency advections.

[41] As for the equatorial band, the seasonal cycle off equator reveals four periods. In the central part of the basin (23°W, Figures 9a and 9b) at the beginning of the year, from February to April, the SST is maximum north of the equator (29.5°C, not shown). During this period, the vertical effects are close to zero, with a strong stratification, and the mixed layer temperature cycle is entirely controlled by the net

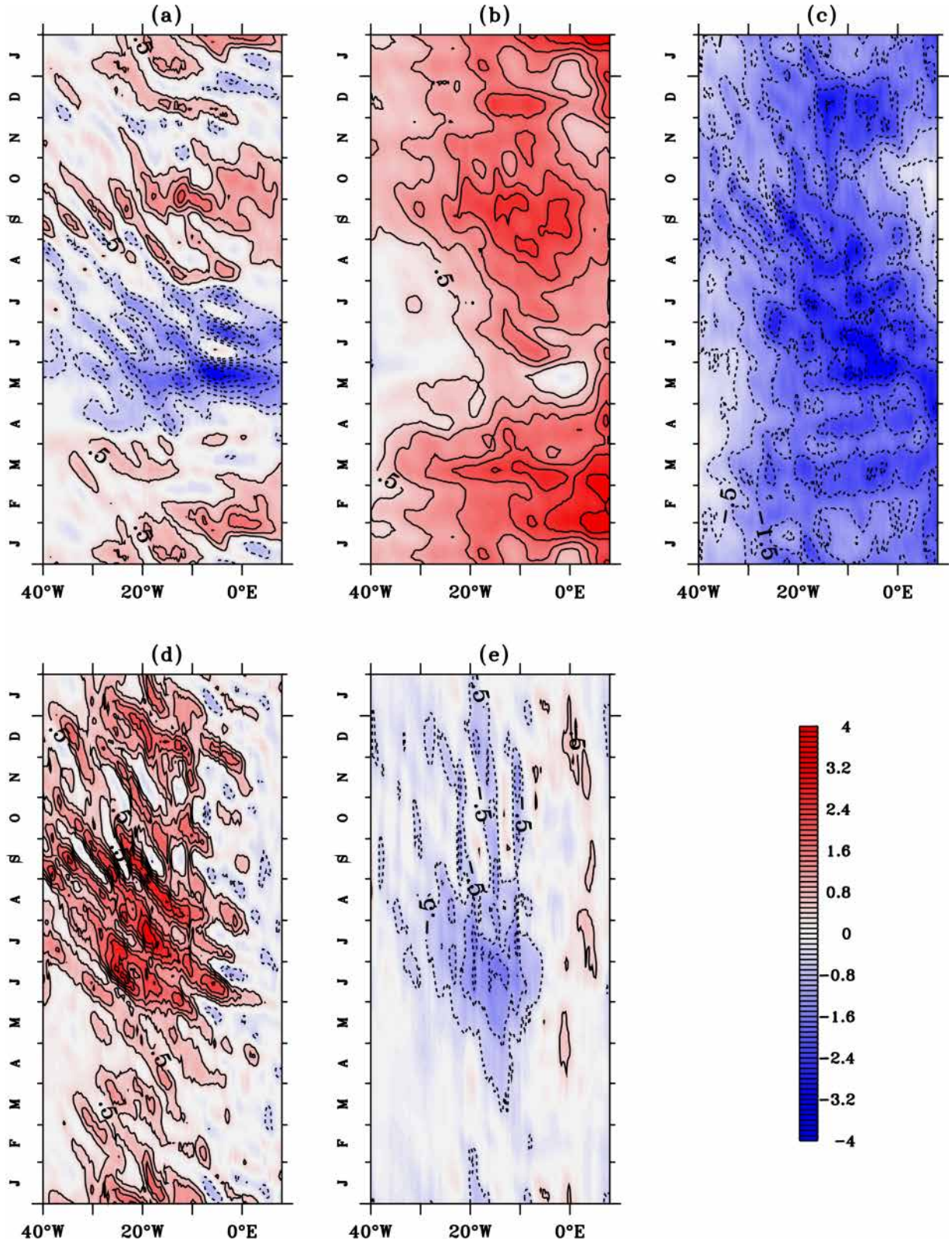

Figure 8. Longitude-time plots along the equator (2°N–2°S average) of 1997–2000 mean seasonal cycles of (a) heat storage, (b) atmospheric forcing, (c) tendencies due to vertical exchanges with the subsurface ocean (sum of vertical advection, vertical diffusion at the base of the mixed layer, and entrainment), (d) eddies (high-frequency horizontal advection plus lateral diffusion), and (e) zonal and meridional advections by low-frequency currents (contours every 0.5°C month^{-1} between −2°C month^{-1} and 2°C month^{-1} and every 1°C month^{-1} after; the thick line is zero). All the trends are smoothed with a 25-day Hanning filter.

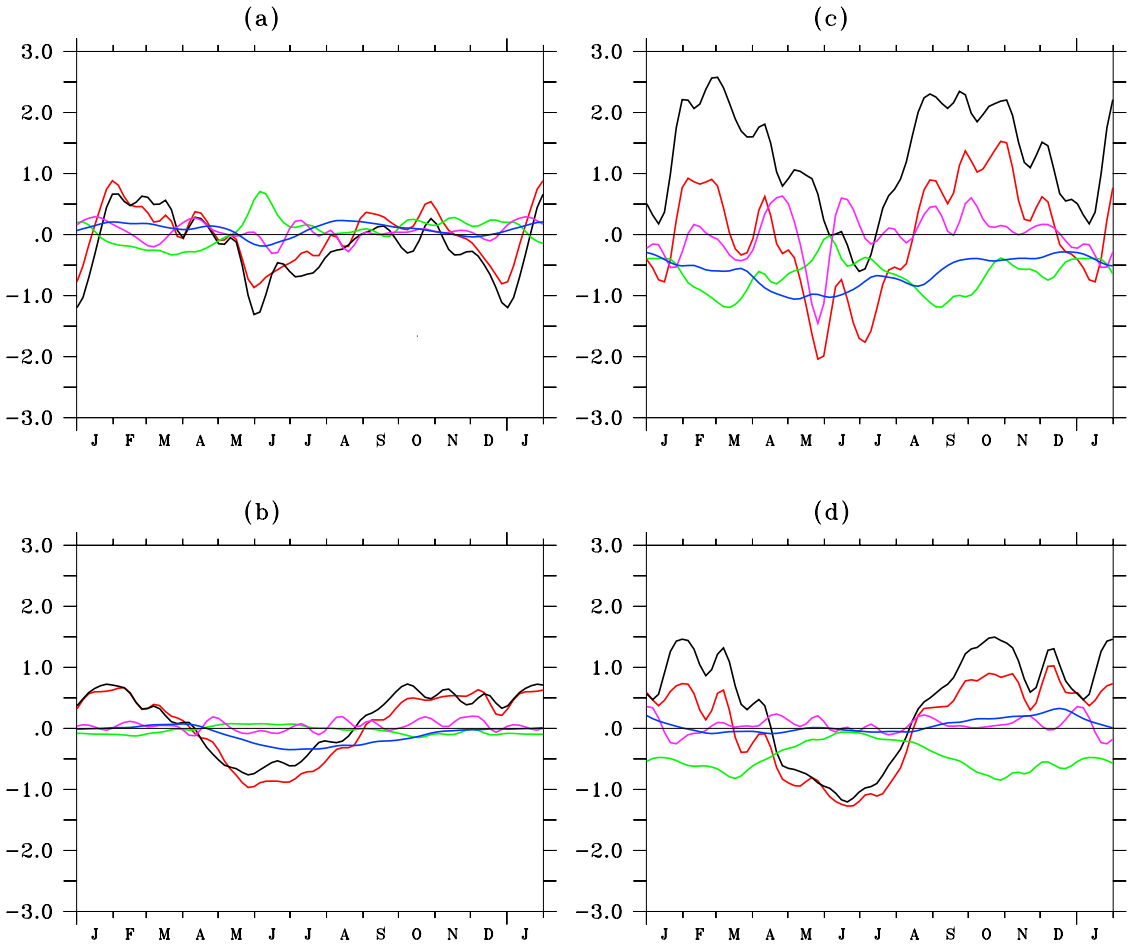

Figure 9. Time plots of 1997–2000 mean seasonal cycles, in °C month^{-1}. Plots (left) at 23°W: (a) 4°N–8°N average and (b) 4°S–8°S average and (right) at 3°E: (c) 4°N–8°N average and (d) 4°S–8°S average. The red line is heat storage, the black line is atmospheric forcing, the green line is subsurface, the purple line is horizontal advection by eddies, and the blue line is zonal and meridional advections by low-frequency currents.

surface forcing. With the increase of the winds in April, the atmospheric forcing decreases and the MLD deepens, in May, and therefore SST also decreases. North of the equator, the increasing heat flux provokes a second warming in boreal fall, and a second cooling in December. South of the equator, the overall trend cycle is annual and is driven essentially by the atmospheric processes with a brief cold period which extends from April to August and a warming tendency over the rest of the year.

[42] East of 10°W, the situation is different. In the northern part of the GG, the seasonal cycle of the wind is more pronounced because of the African monsoon which causes the trade winds to reverse in boreal summer, with a semiannual component corresponding to the two rainy seasons on the African coast. The first takes place in boreal summer, the second occurs in boreal winter. This semiannual signal is very pronounced as an overall trend, in atmospheric forcing, and in subsurface (Figure 9c). The temperature in the ML is entirely driven by the semiannual atmospheric heat flux cycle, although its amplitude is moderated by the cooling action of the subsurface processes, and to a lesser extent by the nearly constant horizontal low-frequency advections. Contrary to what happens in the other locations, the eddies make an important contribution to the heat budget, especially from April to October. In the southern part of the GG (Figure 9d), the mixed layer temperature cycle is dominated by the heat flux cycle.

5. Discussion

[43] We calculated a mixed layer heat budget in the equatorial Atlantic with a similar method as *Vialard et al.* [2001]. Our results in term of dominant processes are comparable.

[44] In the present study, the different contributors to heat budget are found to be very similar to *Jochum et al.* [2005]. For instance, the explicit lateral diffusion is negligible when compared to TIWs, confirming that models resolving TIWs scales are needed to accurately estimate heat budgets in the tropical oceans. However, the mechanisms of equatorial zone warming by TIWs in the Pacific and Atlantic oceans, and their effect on the mixed layer budget are the subject of controversies. On one hand, *Vialard et al.* [2001] with a model in the Pacific, and *Weisberg and Weingartner* [1988]

with observations in the Atlantic, show that TIWs warm the cold tongue through the transport of heat from the north to the cold tongue, to regulate the heat stored in the NECC. On the other hand, *Jochum et al.* [2005] claim that TIWs do not heat from the equatorial cold tongue with heat advected from the warm pool, but draw their heat from the atmosphere. First, *Jochum et al.* [2004] suggest, from a numerical experiment, that eddy-induced horizontal and vertical fluxes almost compensate over a mixed layer of constant depth (20 m), thus preventing TIWs from warming the equatorial cold tongue. On the contrary, there is almost no compensation when TIW-induced horizontal and vertical advections are computed (instead of flux divergences approach which does not allow separating the influence of mass convergence) over a time- and space-varying mixed layer (see *Menkes et al.* [2006] for a thorough discussion). Second, in our model, a particle starting at the surface in the equatorial upwelling is advected away to the north where it encounters the SST front and downwells, escaping from the direct atmospheric forcing while recirculating back to the equator and up in the equatorial waters. Furthermore, while a typical particle entrained in a TIW recirculates, a number of particle from the NECC are entrained into passing vortices associated to the TIWs. These warm particle waters actually do transport heat from the NECC warm waters to the cold tongue (P. Dutrieux, personal communication, 2002). Thus, in our model configuration, there is a direct oceanic heat transport from the NECC to the cold tongue. Yet, it has been demonstrated in observations that the atmosphere is structured at the TIW scales. It is thus likely that the atmosphere indeed retroacts on the ocean heat transport at the TIW scale. However, how this actually occurs is yet to be resolved and would need, from a modeling point of view, the construction of a fully coupled ocean-atmosphere high-resolution model.

[45] Comparisons with studies of the SST heat budgets computed from observations [*Merle*, 1980; *Weingartner and Weisberg*, 1991] in the equatorial Atlantic give qualitatively similar results despite different methodologies. In particular, *Weingartner and Weisberg* [1991] explained the seasonal variations in SST by several different mechanisms, each operating at a different phase of the annual cycle: the rapid decrease in SST in boreal spring and the appearance of the cold tongue was attributed primarily to upwelling-induced cooling by vertical advection; they found an increase in the horizontal advection with the onset of the instability wave season wherein a meridional Reynolds' heat flux convergence resulted in increasing SST, which was then driven by surface heat flux. These results are qualitatively (if not quantitatively) comparable to the present results.

[46] In a recent study, FGCM used in situ temperatures from PIRATA moorings, near-surface drifting buoys, and a blended satellite–in situ SST product to calculate mixed layer temperature evolution in the tropical Atlantic Ocean. Minimum, maximum and mean of the different terms of both heat budgets are presented in Figure 10 (left). The seasonal evolution of the modeled trends (Figure 10, right) can be compared to Figure 5 of FGCM. Except for the contributions of the vertical cooling terms and the low-frequency advections, one can see on Figures 10a, 10b, and 10c the reasonable agreement between the present study and the data in terms of signs, amplitude, mean values, and latitudinal evolution. The major difference between the two heat budgets concerns the process responsible of the cooling: subsurface term (entrainment + vertical advection + vertical diffusion) in the present study and zonal advection by low-frequency currents of FGCM. This difference may originate from the strong residue that is found in FGCM's budget, especially at 10°W, that may be due to an underestimation of the vertical processes estimated from observations. Besides, the importance of the mean zonal advection in observations compared to our model may result from the scarcity of the observations, essentially based on drifters data that rapidly diverge from the equator.

[47] However, the model also has limitations, first the relaxation term added to the ECMWF atmospheric heat fluxes. Figures 10d, 10e, and 10f show the seasonal cycles of the relaxation term (in black dashed lines) and the total net heat flux (ECMWF + relaxation, in black continuous lines). The relaxation term is always positive, whatever the location, in agreement with the previously discussed cold bias in the equatorial modeled SST. This term is necessary everywhere for the mean state, but important for the seasonal cycle only in the eastern part of the basin. It might account either for uncertainties in the ECMWF atmospheric heat fluxes or unresolved dynamics and thermodynamics in the present oceanic model. Comparisons with satellite or in situ data show that ECMWF net heat flux is too weak near the equator. Comparison between PIRATA flux and ECMWF flux also reveals that the primary role of the relaxation term is to bring the ECMWF flux nearer the observed flux. The relaxation term may account in particular for a possible bad representation of the cloudiness over the GG. Furthermore, to illustrate uncertainties due to atmospheric forcing, we have computed the same mixed layer heat budget with another configuration of OPA, ORCA05 (see details of this configuration in work by *de Boyer Montégut et al.* [2006]), which is forced in bulk formulae for heat and salt fluxes. The results are presented on Figure 10 (left). We observed that even though seasonal amplitudes are different (Figures 10a, 10b, and 10c), the relative importances of the terms are the same (Figure 10g), which means that the overall heat balance is unchanged. This suggests that, in spite of the differences in spatial resolution and in the parameterization of lateral diffusion between the two simulations, our results are largely independent of the choice of a specific heat flux data set. This important conclusion holds also for the wind stress as demonstrated in the equatorial Pacific by *Cravatte et al.* [2005]. Secondly, as shown in validation sections, the vertical structure is not exactly simulated by CLIPPER with an underestimation of the MLD in the western part of the basin, and a slightly too diffuse thermocline compared to in situ data. Even if the stratification underestimation leads to an augmentation of the vertical diffusion coefficient (the current shear seems realistic), the too diffusive thermocline tends to underestimate the vertical diffusion and the entrainment, by decreasing the temperature vertical gradient (equation (1)). This underestimation of the cooling should induce warmer SST than observed, which is not the case, suggesting that

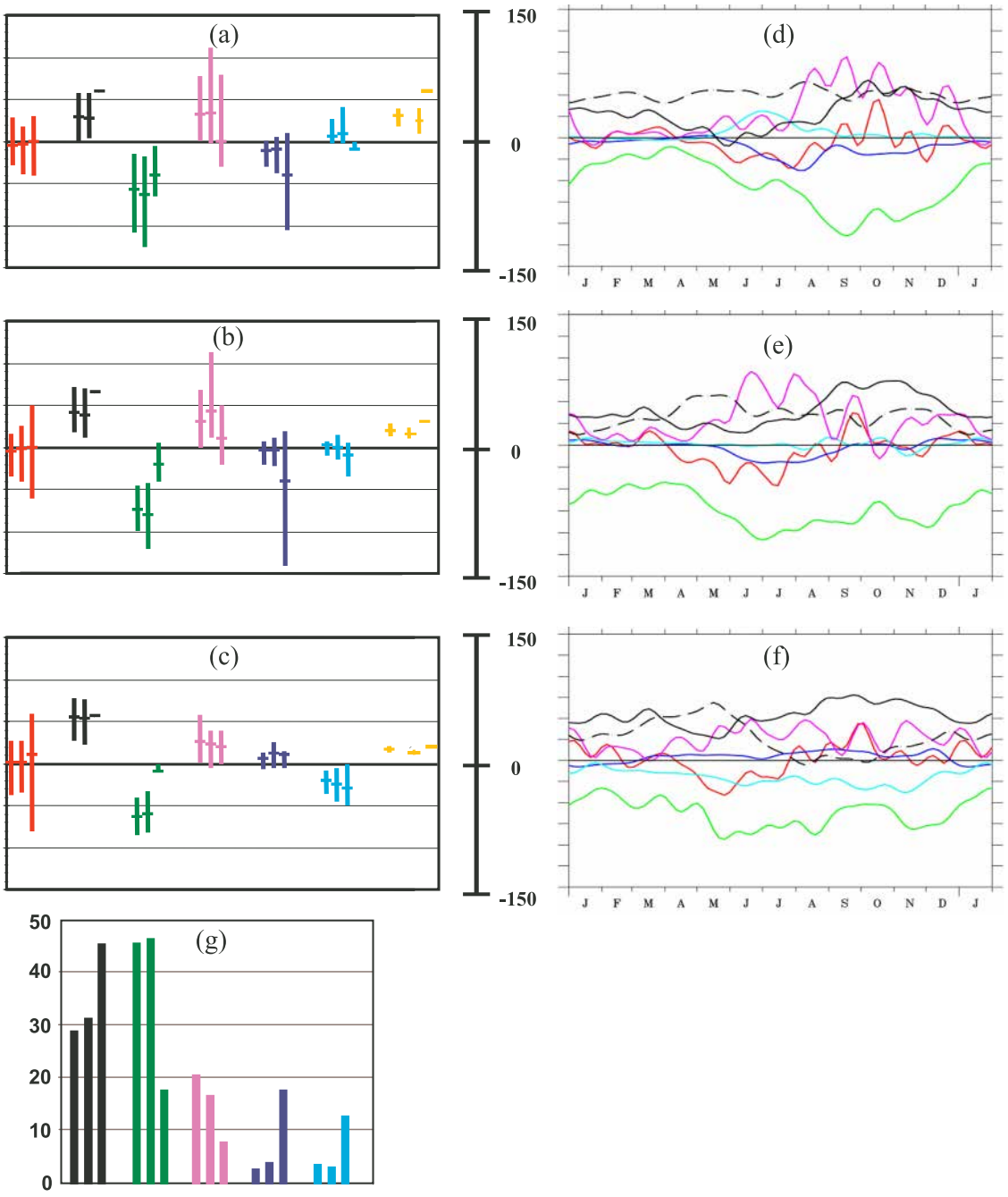

Figure 10. Heat budget annual tendencies (W m^{-2}) and mixed layer depth (m, in yellow) for CLIPPER (left bars), ORCA05 (middle bars) and PIRATA (right bars) at (a) 35°W–0°N, (b) 23°W–0°N, and (c) 10°W–0°N. The PIRATA heat budget values are from *Foltz et al.* [2003]. The bars represent minimum, maximum (vertical bars), and mean (horizontal bars). Seasonal cycle of CLIPPER tendencies around (d) 35°W–0°N, (e) 23°W–0°N, and (f) 10°W–0°N, in W m^{-2}. (g) Relative contributions (%) of the various terms for the total budget in CLIPPER (left bars), ORCA05 (middle bars), and PIRATA (right bars). Heat storage is given in red, forcing is given in black (dashed line is the damping contribution), subsurface is given in green, horizontal advection by eddies is given in purple, zonal advection by low-frequency currents is given in dark blue, and meridional advection by low-frequency currents is given in light blue.

there is not enough warming, from either surface heat fluxes or TIWs. The too shallow MLD cannot explain this surestimation: indeed, if the atmospheric heat fluxes were integrated on a deeper layer, it would decrease their contribution to the mixed layer temperature budget. Finally, another source of uncertainties in our numerical approach is parameterization of the vertical and lateral diffusion, which has been shown to be crucial for the

variability in the Tropical Ocean [*Blanke and Delecluse*, 1993].

6. Summary

[48] In this study, the seasonal cycle of the equatorial mixed layer heat budget is investigated using a numerical simulation of the Tropical Atlantic. A high-resolution ocean general circulation model is used to diagnose the various contributions to a local and closed mixed layer heat budget. The simulation reproduces reasonably well the main features of the circulation and thermal structure of the tropical Atlantic. The modeled closed mixed layer heat budget is decomposed into six terms: the temperature evolution, the atmospheric flux forcing, the vertical processes (sum of vertical diffusion, vertical advection and entrainment), the eddies (regrouping the horizontal high-frequency (<35 days) advection and the lateral diffusion), and the two components (zonal and meridional) of the horizontal advection by low-frequency currents (>35 days). Unlike several other studies, the SST equation is integrated over a time- and space-varying mixed layer.

[49] At a first order, the SST balance at the equator is found to be the result of both cooling by subsurface processes (through vertical mixing at the base of the mixed layer, vertical advection and entrainment), and heating by atmospheric net heat fluxes and eddies (mainly TIWs). The cooling by subsurface processes is strongest in June–August and December when the easterlies are strong. Heating by the atmosphere is maximum in February–March and September–October, whereas the eddies are most active in boreal summer. On the other hand, horizontal advection by low-frequency currents only plays a minor role in the heat budget. Off equator, the sea surface temperature variability is mainly governed by atmospheric forcing all year long, except in the northeastern part of the basin where strong eddies generated at the location of the thermal front significantly contribute to the heat budget in boreal summer.

[50] Comparisons with previously published observational studies show relatively close conformity. However, this study reveals the major role played by the vertical exchanges at the base of the mixed layer that might be partly corresponding to the residue in heat budgets computed from observations. Experiment with higher-vertical resolution will be necessary to study the processes between the ML and the underlying thermocline. In particular, the fact that the MLD and the thermocline variations are not in phase in the eastern part of the basin will be the subject of further research. Moreover, the relaxation term, essential in this oceanic model to simulate the mean state and the seasonal cycle in the cold tongue region, highlights the importance of improving the quality of the atmospheric heat fluxes in the equatorial Atlantic. Cruises dedicated to study of ocean-atmosphere interactions in the GG, as part of the African Monsoon Multidisciplinary Analyses (AMMA) program could be useful in this respect. Besides, more in situ observations are needed to identify and quantify the vertical processes in the upper layer of equatorial oceans.

[51] **Acknowledgments.** We would like to thank Anne-Marie Treguier (LPO, Brest, France) and Jean-Marc Molines (LEGI, Grenoble, France) for the CLIPPER runs. All the computations were performed on IDRIS supercomputers. Special thanks are dedicated to Serena Illig, who brings pertinent contributions to these analyses. We would also like to thank Marchus Jochum; an anonymous reviewer; and the editor, Raghu Murtugudde, for their very useful comments and suggestions.

References

Arhan, M., A. M. Treguier, B. Bourlès, and S. Michel (2006), Diagnosing the annual cycle of the Equatorial Undercurrent in the Atlantic Ocean from a general circulation model, *J. Phys. Oceanogr.*, in press.

Barnier, B., L. Siefridt, and P. Marchesiello (1995), Thermal forcing for a global ocean circulation model using a three-year climatology of ECMWF analyses, *J. Mar. Syst.*, *6*, 363–380.

Blanke, B., and P. Delecluse (1993), Variability of the tropical Atlantic Ocean simulated by a general circulation model with two different mixed layer physics, *J. Phys. Oceanogr.*, *23*, 1363–1388.

Bourlès, B., M. D'Orgeville, G. Eldin, Y. Gouriou, R. Chuchla, Y. DuPenhoat, and S. Arnault (2002), On the evolution of the thermocline and subthermocline eastward currents in the equatorial Atlantic, *Geophys. Res. Lett.*, *29*(16), 1785, doi:10.1029/2002GL015098.

Busalacchi, A. J., and J. Picaut (1983), Seasonal variability from a model of the tropical Atlantic Ocean, *J. Phys. Oceanogr.*, *13*, 1564–1588.

Caltabiano, A. C. V., I. S. Robinson, and L. P. Pezzi (2005), Multi-year satellite observations of instability waves in the tropical Atlantic Ocean, *Ocean Sci. Discuss.*, *2*, 1–35.

Carton, J. A., and Z. X. Zhou (1997), Annual cycle of sea surface temperature in the tropical Atlantic Ocean, *J. Geophys. Res.*, *102*, 27,813–27,824.

Chang, P., R. Saravanan, L. Ji, and G. C. Hegerl (2000), The effect of local sea surface temperatures on atmospheric circulation over the tropical Atlantic sector, *J. Clim.*, *13*, 2195–2216.

Chelton, D. B., F. J. Wentz, C. L. Gentemann, R. A. de Szoeke, and M. G. Schlax (2000), Satellite microwave SST observations of transequatorial tropical instability waves, *Geophys. Res. Lett.*, *27*(9), 1239–1242.

Cravatte, S., C. E. Menkes, T. Gorgues, O. Aumont, and G. Madec (2005), Sensitivity of the modeled dynamics and biogeochemistry of the equatorial Pacific Ocean to wind forcing during the 1997–1999 ENSO, paper presented at the 1st Alexander von Humboldt International Conference on the El Niño Phenomenon and its Global Impact, Eur. Geosci. Union, Guayaquil, Ecuador, 16–20 May.

de Boyer Montégut, C., G. Madec, A. S. Fischer, A. Lazar, and D. Iudicone (2004), Mixed layer depth over the global ocean: An examination of profile data and a profile-based climatology, *J. Geophys. Res.*, *109*, C12003, doi:10.1029/2004JC002378.

de Boyer Montégut, C., J. Vialard, S. S. C. Shenoi, D. Shankar, F. Durand, C. Ethé, and G. Madec (2006), Simulated seasonal and interannual variability of mixed layer heat budget in the northern Indian Ocean, *J. Clim.*, in press.

Du Penhoat, Y., and A. M. Treguier (1985), The seasonal linear response of the tropical Atlantic Ocean, *J. Phys. Oceanogr.*, *15*, 316–329.

Duvel, J.-P., R. Roca, and J. Vialard (2004), Ocean mixed layer temperature variations induced by intraseasonal convective perturbations over the Indian Ocean, *J. Atmos. Sci.*, *61*, 1004–1023.

Foltz, G. R., S. A. Grodsky, J. A. Carton, and M. J. McPhaden (2003), Seasonal mixed layer heat budget of the tropical Atlantic Ocean, *J. Geophys. Res.*, *108*(C5), 3146, doi:10.1029/2002JC001584.

Fontaine, B., P. Roucou, and S. Trzaska (2003), Atmospheric water cycle and moisture fluxes in the West African monsoon: Mean annual cycles and relationship using NCEP/NCAR reanalysis, *Geophys. Res. Lett.*, *30*(3), 1117, doi:10.1029/2002GL015834.

Gibson, J. K., P. Kallberg, S. Uppala, A. Noumura, A. Hernandez, and E. Serrano (1997), ERA description, *ECMWF Re-anal. Proj. Rep. Ser. 1*, 77 pp., Eur. Cent. For Medium-Range Weather Forecasts, Reading, U. K.

Grima, N., A. Bentamy, K. Katsaros, Y. Quilfen, P. Delecluse, and C. Levy (1999), Sensitivity of an oceanic general circulation model forced by satellite wind stress fields, *J. Geophys. Res.*, *104*, 7967–7990.

Hastenrath, S., and J. Merle (1987), Annual cycle of subsurface thermal structure in the tropical Atlantic Ocean, *J. Phys. Oceanogr.*, *17*, 1518–1538.

Houghton, R. W. (1989), Influence of local and remote wind forcing in the Gulf of Guinea, *J. Geophys. Res.*, *94*, 4816–4828.

Houghton, R. W. (1991), The relationship of sea surface temperature to thermocline depth at annual and interannual time scales in the tropical Atlantic Ocean, *J. Geophys. Res.*, *96*, 15,173–15,185.

Houghton, R. W., and C. Colin (1986), Thermal structure along 4°W in the Gulf of Guinea during 1983–1984, *J. Geophys. Res.*, *91*, 11,727–11,739.

Jochum, M., P. Malanotte-Rizzoli, and A. J. Busalacchi (2004), Tropical instability waves in the Atlantic Ocean, *Ocean Modell.*, *7*, 145–163.

Jochum, M., R. Murtugudde, R. Ferrari, and P. Malanotte-Rizzoli (2005), The impact of horizontal resolution on the tropical heat budget in an Atlantic Ocean model, *Clim, J.*, *18*, 841–851.

Legeckis, R., and G. Reverdin (1987), Equatorial long waves in the Atlantic Ocean in 1983, *J. Geophys. Res.*, *92*, 2835–2842.

Le Traon, P. Y., F. Nadal, and N. Ducet (1998), An improved mapping method of multi-satellite altimeter data, *J. Atmos. Oceanic Technol.*, *15*, 522–534.

Li, T., and S. G. H. Philander (1997), On the seasonal cycle of the equatorial Atlantic Ocean, *J. Clim.*, *10*, 813–817.

Madec, G., P. Delecluse, M. Imbard, and C. Levy (1998), OPA8.1 Ocean General Circulation Model reference manual, *Notes du Pôle de Modélisation IPSL 11*, Inst. Pierre-Simon Laplace, Paris, Dec.

Menkes, C. E., J. Vialard, S. C. Kennan, J. P. Boulanger, G. Madec, and K. Rodgers (2006), A modelling study of the three-dimensional heat budget of tropical instability waves in the equatorial Pacific, *J. Phys. Oceanogr.*, in press.

Merle, J. (1980), Seasonal heat budget in the equatorial Atlantic Ocean, *J. Phys. Oceanogr.*, *14*, 1216–1225.

Michel, S., and A. M. Treguier (2002), Sensitivity of the equatorial undercurrent to mixing parametrizations in the CLIPPER model, *Rap. DRO/LPO 02-16*, 35 pp., Dir. des Rech. Oceaniques/Lab. de Phys. des Oceans, Brest, France, Oct.

Mitchell, T. P., and J. M. Wallace (1992), The annual cycle in equatorial convection and sea surface temperature, *J. Clim.*, *5*, 1140–1156.

Okumura, Y., and S. P. Xie (2004), Interaction of the Atlantic equatorial cold tongue and African monsoon, *J. Clim.*, *17*, 3588–3601.

Okumura, Y., and S. P. Xie (2005), Overlooked November–December cooling of the equatorial Atlantic and its effects on interannual variability and predictability, paper presented at CLIVAR Atlantic Meeting, Clim. Variability and Predict., Miami, Fla., Jan.

Paulson, C. A., and J. J. Simpson (1977), Irradiance measurements in the upper ocean, *J. Phys. Oceanogr.*, *7*, 952–956.

Philander, S. G. H., and R. C. Pacanowski (1986), The mass and heat budget in a model of the tropical Atlantic Ocean, *J. Geophys. Res.*, *91*, 14,212–14,220.

Reynolds, R. W., and T. M. Smith (1994), Improved global sea surface temperature analyses using optimal interpolation, *J. Clim.*, *7*, 929–948.

Richards, K. J., and N. R. Edwards (2003), Lateral mixing in the equatorial Pacific: The importance of inertial instability, *Geophys. Res. Lett.*, *30*(17), 1888, doi:10.1029/2003GL017768.

Richardson, P. L., and T. K. McKee (1984), Average seasonal variation of the Atlantic equatorial currents from historical ship drifts, *J. Phys. Oceanogr.*, *14*, 1226–1238.

Servain, J., A. J. Busalacchi, M. J. McPhaden, A. D. Moura, G. Reverdin, M. Vianna, and S. E. Zebiak (1998), A pilot research moored array in the tropical Atlantic (PIRATA), *Bull. Am. Meteorol. Soc.*, *79*, 2019–2031.

Treguier, A. M., B. Barnier, A. P. de Miranda, J. M. Molines, N. Grima, M. Imbard, C. Messager, T. Reynaud, and S. Michel (2001), An eddy-permitting model of the Atlantic circulation: Evaluating open boundary conditions, *J. Geophys. Res.*, *106*, 22,115–22,130.

Vauclair, F., and Y. du Penhoat (2001), Interannual variability of the upper layer of the tropical Atlantic Ocean from in situ data between 1979 and 1999, *Clim. Dyn.*, *17*, 527–546.

Vialard, J., C. Menkes, J. P. Boulanger, P. Delecluse, E. Guilyardi, M. J. McPhaden, and G. Madec (2001), A model study of oceanic mechanisms affecting equatorial Pacific sea surface temperature during the 1997–98 El Nino, *J. Phys. Oceanogr.*, *31*, 1649–1675.

Weingartner, T. J., and R. H. Weisberg (1991), A description of the annual cycle in sea surface temperature and upper ocean heat in the equatorial Atlantic, *J. Phys. Oceanogr.*, *21*, 83–96.

Weisberg, R. H., and T. J. Weingartner (1988), Instability waves in the equatorial Atlantic Ocean, *J. Phys. Oceanogr.*, *18*, 1641–1657.

Xie, S.-P., and J. A. Carton (2004), Tropical Atlantic variability: Patterns, mechanisms, and impacts, in *Earth Climate: The Ocean-Atmosphere Interaction*, *Geophys. Monogr. Ser.*, vol. 147, edited by C. Wang, S.-P. Xie, and J. A. Carton, pp. 121–142, AGU, Washington, D. C.

Yu, L., R. A. Weller, and B. Sun (2004), Improving latent and sensible heat flux estimates for the Atlantic Ocean (1988–99) by a synthesis approach, *J. Clim.*, *17*, 373–393.

G. Caniaux, Centre National Recherche Meteorologique, 42, av. G. Coriolis, F-31057 Toulouse, France.

Y. du Penhoat, F. Marin, and A.-C. Peter, Laboratoire d'Etudes en Géophysique et Océanographie Spatiales, Centre National d'Etudes Spatiales, CNRS, Institut de Recherche Pour le Développement, Université Paul Sabatier, 14, av. Edouard Belin, F-31400 Toulouse, France. (anne.charlotte@peter.vu)

M. Le Hénaff, A. Lazar, C. E. Menkes, and J. Vialard, LOCEAN, Institut de Recherche Pour le Développement, CNRS, Université Pierre et Marie Curie, Museum National d'Histoire Naturelle, 4, place Jussieu, F-75252 Paris Cedex 05, France.